Results from the H1 Experiment at HERA

A. De Roeck

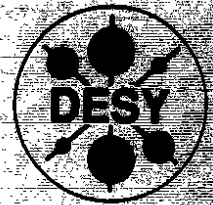*Deutsches Elektronen-Synchrotron DESY, Hamburg*

Results from the H1 Experiment at HERA *

A. De Roeck

Deutsches Elektronen-Synchrotron DESY, Hamburg

ABSTRACT

New results from the H1 experiment at HERA on photoproduction, deep inelastic scattering and search for exotic particles are presented. Clear evidence is found for hard scattering in photoproduction interactions. Jets have been observed and used to examine the x_γ distribution, indicating the need for a gluonic component in the photon. Hadronic final states and jet cross sections have been measured in deep inelastic scattering. A class of deep inelastic events with diffractive characteristics has been observed. The proton structure function $F_2(x, Q^2)$ has been measured in the new Bjorken-x region $10^{-4} < x < 10^{-2}$ and is found to rise with decreasing x. New limits for leptoquarks, squarks and excited electrons have been deduced.

1 Introduction

On the 31st of May 1992 the first ep collisions were produced in the H1 and ZEUS experiments at the newly commissioned high energy collider HERA, in Hamburg, Germany. HERA collides –for the first time– 26.7 GeV electrons on 820 GeV protons, yielding a centre of mass energy of 296 GeV. The H1 experiment has an almost 4π detection coverage for the particles produced in the interaction. The collaboration consists of about 340 physicists from 36 institutes. During '92 H1 collected a data sample corresponding to an integrated luminosity of about $25nb^{-1}$. The results reported in this paper are based on these data. At the end of 1993 a total of 500 nb^{-1} usable for physics analysis has been accumulated by the H1 experiment. More details on the performance of HERA are given in [1].

The kinematics of the inclusive ep scattering process $ep \rightarrow eX$ at fixed centre of mass energy, $\sqrt{s}$, is determined by two independent variables, conventionally chosen to be two of x, y and Q^2. The H1 experiment can measure both the scattered electron and the hadronic final state produced between the struck quark and the proton remnant, thus the collision kinematics can be determined from electron variables, hadronic variables or a mixture of both.

The kinematical variables are defined as follows:

$$Q^2 = -q^2 = -(p_e - p_l)^2, x = \frac{Q^2}{2P.q}, y = \frac{P.q}{P.p_e}, \quad (1)$$

where Q^2 is the four-momentum transfer squared, x the Bjorken-x, and y the fraction of the energy transfered to the proton in the proton rest system. In these definitions p_e, p_l and P denote the four momenta of the incoming and scattered lepton and the incoming proton respectively. At HERA the centre of mass energy squared $s = 4E_e E_p = 87\,600$ GeV^2, with E_e and E_p the energy of the incoming electron and proton respec-

tively. Since $Q^2 = xys$, x values down to $\sim 10^{-4}$ in the deep inelastic regime can be accessed at HERA.

The kinematic variables in charged lepton nucleon scattering are traditionally determined from the angle θ_e, and the energy of the scattered lepton, E'_e, through the relations

$$Q^2 = 4E_e E'_e \cos^2(\frac{\theta_e}{2}), \quad y = 1 - \frac{E'_e}{E_e}\sin^2(\frac{\theta_e}{2}) \quad (2)$$

and then x can be determined as $x = Q^2/(sy)$. Polar angles are measured relative to the proton beam direction, termed the forward direction in the following.

In this paper recent results are reported on photoproduction interactions, deep inelastic scattering and exotic particle searches. For photoproduction interactions, i.e. interactions with $Q^2 \simeq 0$ HERA allows the study of collisions with a centre of mass energy approximately one order of magnitude larger than presently achieved in fixed target experiments. Due to this increase in energy hard scattering in photon-proton collisions is expected to become clearly visible. This leads to the production of jets, which can be used for detailed QCD tests and to derive information on the partonic structure of the photon. Data in the region of large $Q^2(> \text{few } GeV^2)$, the so called deep inelastic scattering (DIS) region, have been used to explore the proton structure for the first time at x values down to $\sim 10^{-4}$. Thus HERA enters a new kinematic region where it has been speculated that new physics may be observed[2]. Further, in the study of the hadronic final state in DIS, a class of events was observed which have a large rapidity gap between the current jet and the proton remnant, and may be explained by a diffractive like mechanism for this interaction. Finally, a search for exotic particles was performed. HERA is particularly suited for production of s-channel resonances from the fusion of 2 incoming partons (i.e. electron with a quark or gluon from the proton for leptoquarks and leptogluons respectively) or the electron with an exchanged boson (e.g. to

---

produce excited leptons), since the full centre of mass energy of the collision can be used to produce these states.

2 The H1 Detector

A detailed description of the H1 detector and its performance can be found in [3]. Here we give a brief overview. The detector is shown in Fig. 1.

Charged particle tracks are measured in a central tracker (CT), a forward tracker (FT), and a backward proportional chamber (BPC). The central tracking detector consists of two large jet drift chamber modules, two z drift chambers and two multiwire proportional chambers for triggering. Its angular acceptance is $15^0 - 165^0$. The forward tracking detector accepts tracks between 7^0 and 25^0. It consists of three modules of drift and multiwire proportional chambers. The BPC has 4 wire planes and an angular acceptance of $155^0 - 175^0$. A superconducting coil provides a uniform magnetic field of $1.15\ T$ in the tracking region which allows the determination of charged particle momenta. The vertex position of an interaction is determined on an event by event basis from tracks reconstructed in the CT and FT, originating from the interaction region. The presently achieved resolutions for charged track parameters are $\sigma_{r\phi} = 170\mu m$ and $\sigma_z = 2mm$ for the CT and $\sigma_{r\phi} = 170\mu m$ and $\sigma_{xy} = 210\mu m$ for the FT.

The tracking detectors are surrounded by calorimeters. The main component is a large Liquid Argon calorimeter (LAr) [4] supplemented by a Backward Electromagnetic Calorimeter (BEMC) and in the forward region by a Plug calorimeter.

The LAr calorimeter consists of an electromagnetic section with lead absorber and a hadronic section with stainless steel absorber. The total depth of the electromagnetic part varies between 20 and 30 radiation lengths whereas the total depth of both calorimeters varies between 4.5 and 8 interaction lengths. The LAr calorimeter covers the angular range between 4° and 153°. The calibration of the LAr calorimeter segments has been obtained from test beam measurements using electrons and pions [3,4,5]. The electromagnetic energy scale is verified to a 3% accuracy in the H1 detector by comparing the measured track momentum of electrons and positrons with the corresponding energy deposition in the calorimetric cells. The absolute scale of the hadronic energy is presently known to 7% as determined from studies of the p_T balance for deep inelastic scattering events.

The BEMC is made of 88 lead/scintillator sandwich stacks, each with a depth of 22 radiation lengths, cor-
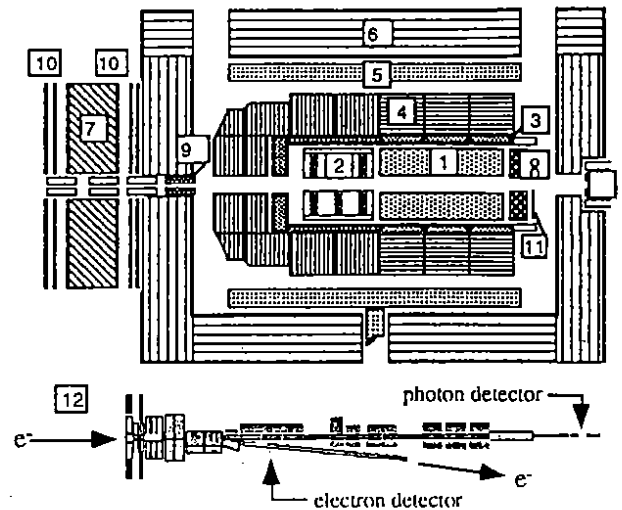

Figure 1: Schematic view of the H1 detector; protons come from the right and electrons come from the left. The components shown are: 1) Central tracking chambers 2) Forward tracking chambers 3) Electromagnetic calorimeter (LAr) 4) Hadronic calorimeter (LAr) 5) Superconducting coil 6) Instrumented iron 7) Forward muon toroid magnet 8) Electromagnetic calorimeter (BEMC) 9) Plug calorimeter 10) Forward muon chambers 11) Time of Flight scintillator (TOF) 12) Luminosity monitor.

responding to about one interaction length. It covers the angular range of $153^0 < \theta_e < 176^0$. A 1.5 cm space resolution for the reconstructed centre of gravity of an electromagnetic cluster has been achieved. The relative calibration of the BEMC stacks and the energy dependent terms of its resolution are determined from test beam measurements. The absolute energy scale and the constant term of the BEMC resolution are determined using deep inelastic scattering events exploiting the redundancy in the measurement of the kinematical variables. The energy scale of the BEMC is known to 2% and its resolution is described by $\sigma(E'_e)/E'_e = 0.1/\sqrt{E'_e} \oplus 0.42/E'_e \oplus 0.03$, where E'_e is in GeV.

The calorimeters are surrounded by an iron structure, which is instrumented with streamer tubes to act as a backing calorimeter and muon filter. The forward region is equiped with a forward muon spectrometer, consisting of a toroidal magnet and drift chambers. The total angular coverage of the H1 detector for muons is $4^o - 171^o$.

Electrons and photons emitted at very small angles with respect to the incoming electron direction are measured in an electron and a photon tagging calorimeter. These detectors are located 33 and 103 m downstream of the interaction point and have angular acceptances below 5 $mrad$ and 0.5 $mrad$, respectively. The electron

and photon taggers are designed to detect the $e - \gamma$ coincidences from the low Q^2 elastic radiative collisions $e + p \rightarrow e + \gamma + p$, used to measure the luminosity. The photon and electron taggers further allow us to study the size of the radiative corrections and the size of the photoproduction background to deep inelastic scattering.

In 1992 HERA was operated with 10 electron and 10 proton bunches, separated by 96 ns. Nine bunches were colliding, one electron and one proton bunch – termed pilot bunches – had no collision partner. The interaction region extends along the beam line with a $\sigma_z \simeq 25$ cm, determined by the length of the proton bunch.

3 Photoproduction

Real photons can interact with matter *directly* through the pointlike coupling of this gauge particle with partons of the hadrons, or via the so called *hadronic* or *resolved* component of the photon. The latter is known for about 30 years and is phenomenologically described by the Vector Dominance Model (VDM). Here the photon is pictured to couple and fluctuate into a $\rho, \omega, \phi...$ vector meson which has the same quantum numbers as the photon. In this case the photon-hadron collision follows the same phenomenology as a hadron-hadron collision. Further, on top of the VDM contribution, this hadronic component is expected to have an additional so called anomalous component which results from the direct splitting of the photon in a $q\bar{q}$ pair.

The interactions of real photons with matter have been studied in fixed target experiments with photon beams, and in $\gamma\gamma$ interactions at e^+e^- colliders. However, the different components of the $\gamma - p$ interaction have not yet been unambiguously isolated.

At HERA almost real photoproduction interactions are produced by ep interactions involving a low Q^2 photon radiated by the electron. Due to the colliding beam environment, centre of mass energies of 200 GeV can be reached for almost real $\gamma - p$ collisions, roughly one order of magnitude larger than what has been reached so far in fixed target experiments. The large centre of mass energy should allow a clean separation of the resolved and direct components and, similar to high energy hadronic interactions, clear jet production and jet structures should become visible. Further, the total photoproduction cross section at these energies is an important measurement, due to speculations based on measurements from cosmic air showers[6]. These measurements have shown an anomalously high muon component in photon induced air showers in the PeV energy range in the laboratory frame. This has lead to predic-

tions for the total photoproduction cross section in the HERA energy region which ranged from 100 to 700 μb.

For all $\gamma - p$ analyses below, events were selected for which the scattered electron is detected by the downstream electron tagger calorimeter. This limits the acceptance to $3 \cdot 10^{-8}$ $GeV^2 < Q^2 < 10^{-2}$ GeV^2 and 150 $GeV < W_{\gamma p} < 250$ GeV, where $W_{\gamma p}$ is the centre of mass energy of the $\gamma - p$ collision. More details are given in [7,8].
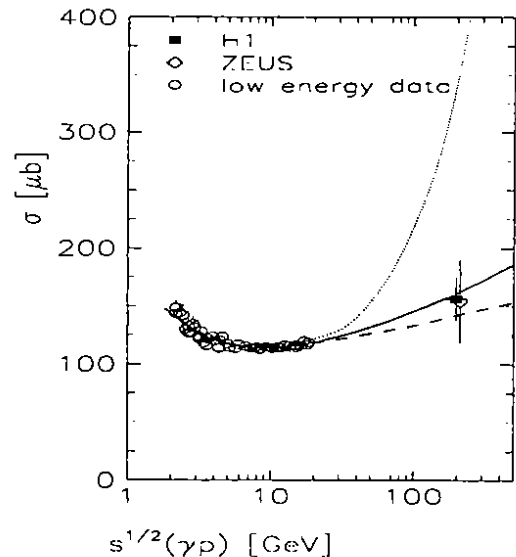

Figure 2: Energy dependence of the total γp cross section. Data from H1 (square) and ZEUS (diamond) are compared to model predictions from [11] (solid) and [12] (dashed). The dotted line is obtained with the PYTHIA Monte Carlo using the ansatz $\sigma = \sigma^{soft} + \sigma^{jet}(s)$ for $\hat{p}_t^{min} = 1.4$ GeV/c.

3.1 Total Cross Section

The total photoproduction cross section has been derived at the centre of mass energy of 197 GeV, from the measured ep cross section, using the Weizsäcker-Williams approximation[9] for the photon flux. Events were selected having a clear vertex in the interaction region and the scattered electron detected in the electron tagger $33m$ downstream the H1 detector. The total cross section measurement is shown in Fig. 2 together with the lower energy data and the ZEUS measurement [10]. The measured value is $156\pm2(stat)\pm18(syst)$. The systmatic error is dominated by the acceptance corrections for photoproduction events in the main detector. The total photoproduction cross section is found to rise only weakly with the increasing centre of mass energy, as predicted by Regge inspired models [11,12].
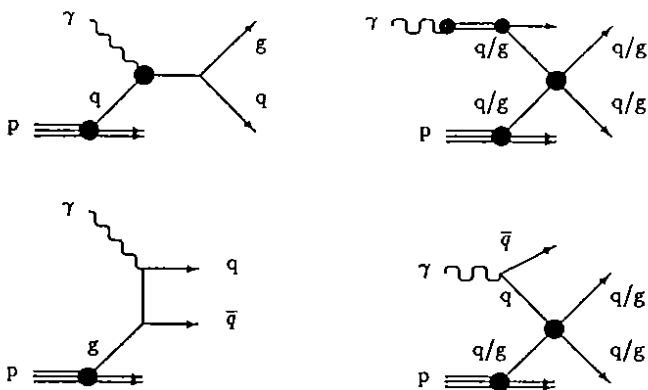
3

Figure 3: Hard γp processes: left part with direct processes QCD Compton and photon gluon fusion; right part with resolved processes from the VDM and anomalous component.

3.2 Hard Scattering

Hard scattering in $\gamma - p$ interactions is expected from partonic collisions between quarks and gluons of the incident proton and the resolved photon, and from the direct production diagrams (boson gluon fusion and QCD Compton scattering). The processes are depicted in Fig. 3. For resolved collisions this picture leads to the introduction of a "photon structure function", describing probabilities for finding partons in the photon with a certain momentum fraction of the photon x_γ.

To establish the presence of hard processes, we study the collimation of tracks as a function of the total transverse energy E_T of the event. As the E_T increases, one expects more pronounced jet formation, leading to clusters of nearby tracks. This is illustrated in Fig. 4 where the p_T flow as a function of $\Delta\phi$, the distance in azimuthal angle with respect to the highest p_T track, is histogrammed for different E_T intervals. Soft events show no structure in the $\Delta\phi$ distribution, while for events with $E_T > 20$ GeV particles clearly prefer a back-to-back cluster configuration.

Another characteristic feature for a hard scattering process is expected to be observed in the inclusive p_T spectrum of charged particles. The spectrum is shown in Fig. 5a for charged particles in the pseudorapidity interval $|\eta| < 1$, with $\eta = -\ln(\tan(\theta/2))$. The data are corrected for detector acceptance effects. A clear high p_T tail is seen, indicating the presence of hard scattering. A next to leading order calculation [13] is compared to the data, showing a very good agreement
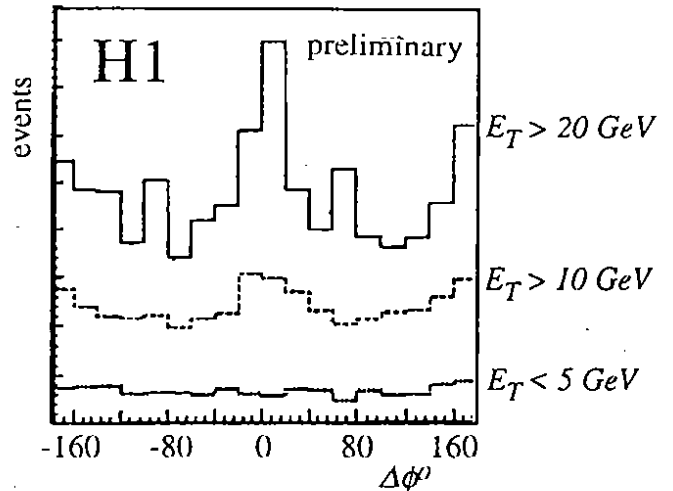

Figure 4: Distribution of the distance $\Delta\phi$ in azimuth ϕ of charged tracks in an event from the leading p_T charged track as a function of calorimeter E_T threshold. ($E_T < 5$ GeV: dotted, $E_T > 10$ GeV: dashed, $E_T > 20$ GeV: solid line).

Fig 5b shows the $p\bar{p}$ data at $\sqrt{s} = 200 GeV$. The high p_T tail in $\gamma - p$ interactions is clearly larger, indicating the presence of extra non-VDM contributions to the $\gamma - p$ cross section.

The next step towards establishing hard scattering in $\gamma - p$ interactions is to look for jets. The single inclusive jet spectra as function of E_T and η have been measured[14]. Jets were selected using a cone algorithm, within the range $-1 < \eta < 1.5$ and $E_T > 7 GeV$. In Fig 6a. the ep jet cross section, corrected to the hadron level, is shown as function of E_T. The data follow an $E_T^{-5.5}$ dependence. Also shown are LO QCD predictions calculated using PYTHIA [15] for different assumptions for the parton distributions in the photon. The η dependence of the jet cross section is shown in Fig 6b. None of the models describes the η dependence well.

The jet kinematics can be used to determine the momentum fraction x_γ of the parton in the photon involved in the hard scattering collision. Indeed, for 2 jet events

$$ x_\gamma = \frac{E_T^1 e^{-\eta^1} + E_T^2 e^{-\eta^2}}{2yE_\gamma}, \qquad (3) $$

where the indices refer to the first and second jet.

About 800 2-jet events were selected, with the requirement that each jet has an E_T of at least 5 GeV. The jets were accepted within the range $|\eta| < 2.5$. The data, not corrected for detector smearing, are shown in Fig. 7 and compared with LO QCD calculations for
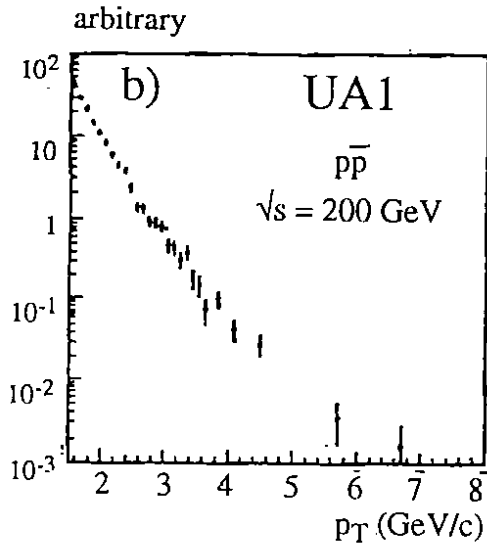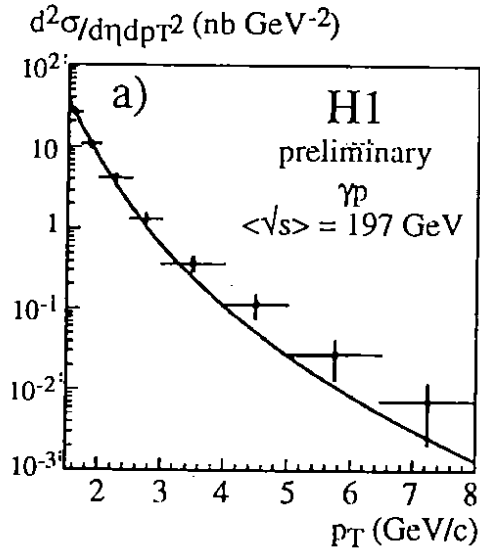
4

Figure 5: a) Inclusive charged track p_T ep cross section for tracks with $\eta < 1$, together with a NLO QCD calculation [13] (shape comparison only); b) The same spectrum measured in $p\bar{p}$ interactions (shape comparison only).
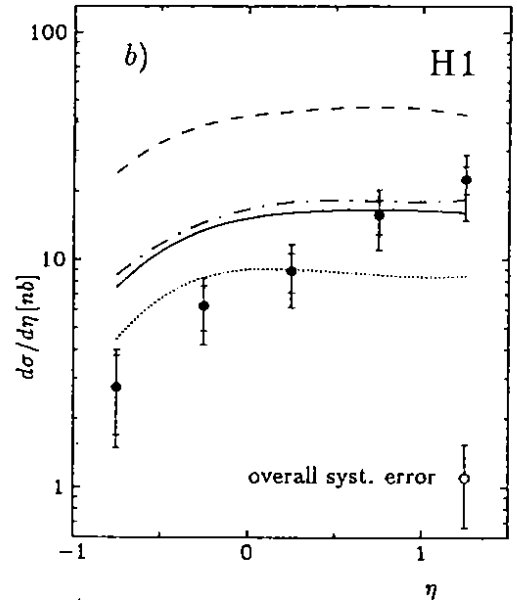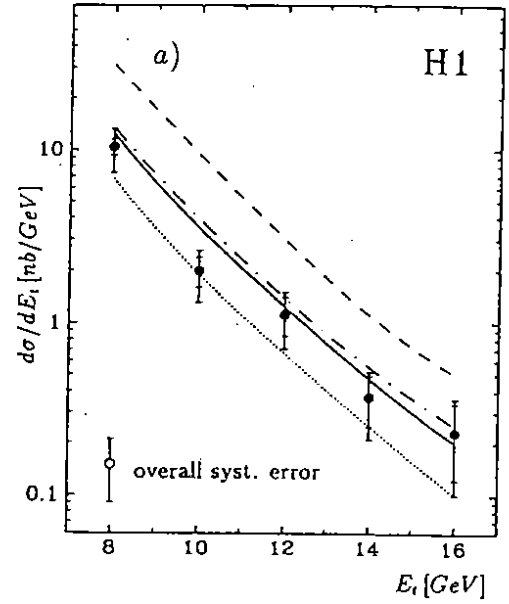
Figure 6: a) Inclusive jet E_t spectrum integrated over the pseudorapidity interval $-1.0 < \eta < 1.5$; b) inclusive jet η spectrum for jets with $E_T > 7\ GeV$. The inner error bars represent the statistical errors, the outer error bars the statistical and systematic errors added in quadrature. The overall systematic uncertainty of 40% is shown separately. The curves represent the leading-order calculations in the framework of the PYTHIA event generator using the photon structure functions LAC-3 (dashed line), LAC-2 (dashed-dotted line), GRV-LO (full line) and GRV-LO, but excluding the gluons originating from the photon (dotted line).
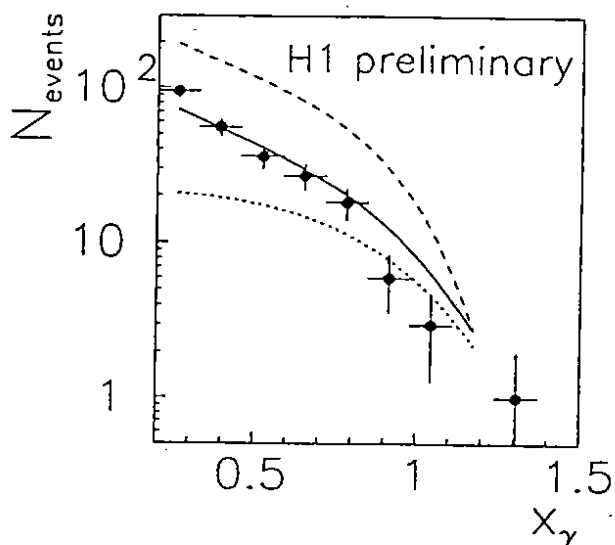
5

Figure 7: Momentum fraction of partons from photons. Points are H1 measurements, curves are leading order QCD calculations as in Fig. 6.

4 Hadronic Final States in DIS

Previous lower energy lepton-nucleon DIS measurements [18,19,20] have shown that the topological characteristics of the hadronic final state can only be described if QCD corrections are made to the naive parton model. In particular, the observed event shapes and the transverse momentum distributions of final state hadrons were described in terms of $O(\alpha_s)$ QCD matrix elements, additional effects of soft gluons, and fragmentation [21]. Quantitative studies of jet production have so far been carried out extensively in e^+e^- and $p\bar{p}$ collisions. Recently, a first multi-jet analysis in fixed target deep inelastic μN scattering was reported [20]. At HERA the centre of mass energy is large and multi-jet events are expected to become clearly visible. A comprehensive report on hadronic final states is given in [22].
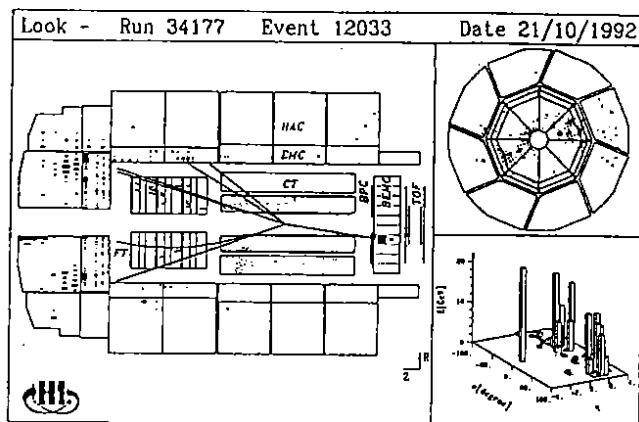
different assumptions for the parton distributions in the photon. These predictions were calculated using the PYTHIA Monte Carlo event generator. Generated events were simulated with a detailed simulation program of the H1 detector and then reconstructed with the same reconstruction program as used for the data. The parton distributions used include the LAC3[16] (dashed line) and GRV[17] (full line) distributions. Both parton distributions successfully describe the photon structure function data, measured in e^+e^- 2-photon collisions. The 2 photon collisions provide mainly information on the quark distributions in the photon, but leave the gluon distribution largely unconstrained. Therefore the assumptions for the gluon distribution prescribed by different parton parametrizations of the photon differ wildly. The LAC3 distribution assumes a large gluon component at high x_γ. This scenario is clearly disfavoured by the data. The dotted curve shows the prediction assuming no gluons from the photon are involved in the interactions. This prediction undershoots the data at low x_γ where we expect the gluons to become important. This clearly shows that this measurement is sensitive to the gluonic component of the photon. Similar conclusions can be made from the jet rates shown in Fig. 6. Clearly, the next task will be to *extract* the gluon distribution from the 2-jet data in $\gamma - p$ collisions.

Figure 8: A deep inelastic event in the H1 detector with a 2+1 jet configuration observed in the final state.

4.1 Jet Rates

In the quark parton model (QPM), one jet arises from the struck quark scattering into the detector, while the proton remnant leads to another jet. This is called a "1+1" jet event configuration. The proton remnant is generally lost in the beam pipe. Due to QCD processes to $O(\alpha_s)$, such as gluon radiation in the initial or final state or photon-gluon fusion, a further jet appears, giving rise to 2+1 jet events. Fig. 8 shows a 2+1 jet event in the H1 detector. Two well separated jets are visible in the forward part of the detector and in the energy flow plot, with a possible third jet close to the proton remnant direction.
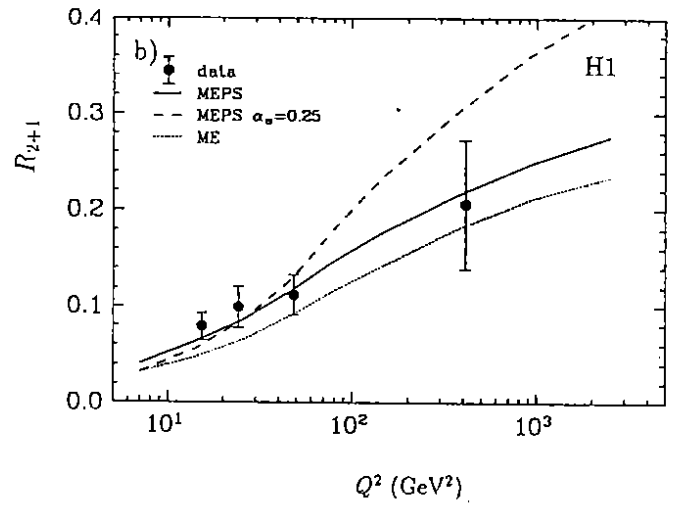
6
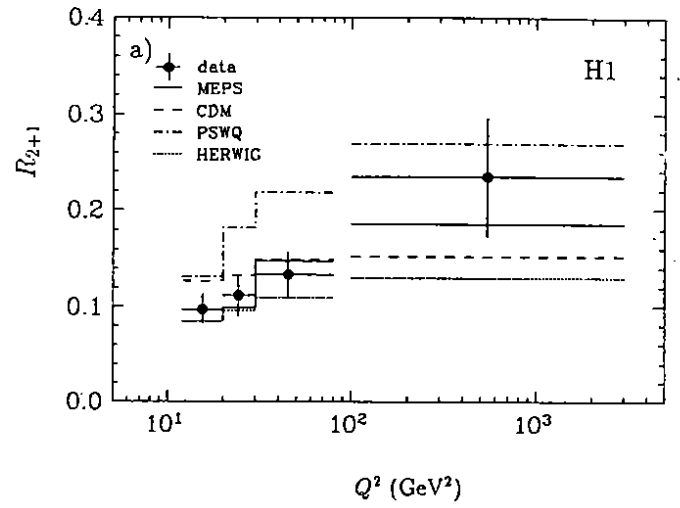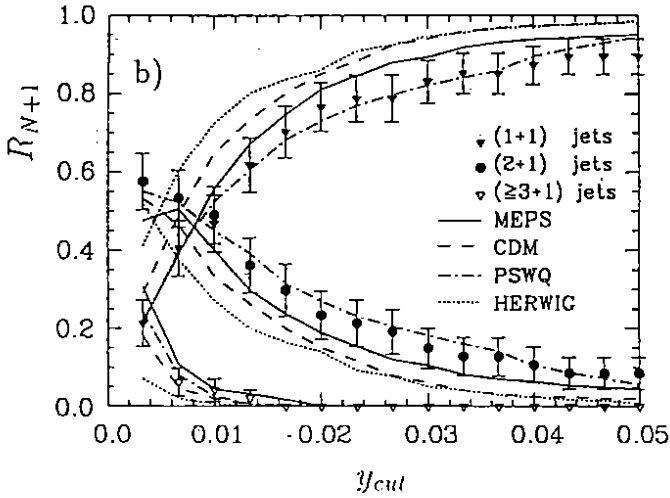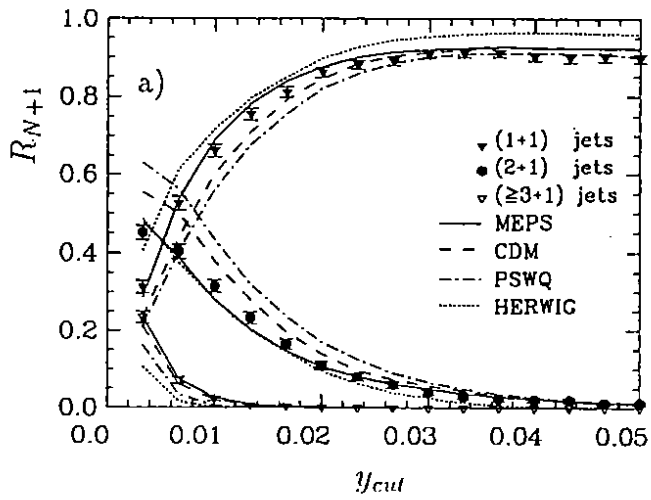
Figure 9: Fractional jet rates versus the jet resolution parameter y_{cut} for (a) the low and (b) the high Q^2 event sample compared to the predictions of different QCD models.

Figure 10: a) Uncorrected (2+1) jet fraction R_{2+1} at $y_{cut} = 0.02$ versus Q^2 compared with different QCD based models: MEPS, CDM, PSWQ and HERWIG. b) (2+1) jet fraction R_{2+1} at $y_{cut} = 0.02$ versus Q^2, corrected for detector bias in comparison with the MEPS model with a running α_S and a constant $\alpha_S = 0.25$, and also with the matrix elements but no parton showers (ME model). The data are plotted at the corrected $< Q^2 >$ per bin.

In this analysis we make use of an (almost) Lorentz invariant cluster algorithm, referred to as the JADE algorithm [23]. In this scheme resolution (y_{cut}) dependent jet multiplicities are determined by calculating scaled invariant masses y_{ij} defined as

$$y_{ij} = \frac{m_{ij}^2}{W^2}, \qquad \text{with} \qquad m_{ij}^2 = 2E_iE_j(1 - \cos\theta_{ij}),$$

that is, neglecting the masses of clusters i and j. Here the invariant mass of the hadronic system W is chosen as scale. Calorimeter cells are combined into clusters starting with the smallest invariant mass pair. Clustering is repeated until y_{ij} is above the jet resolution parameter y_{cut} for all clusters. The remaining clusters are counted as jets. The loss of a large fraction of the proton remnant jet in the beampipe is compensated in the jet algorithm by introducing a pseudoparticle carrying the missing longitudinal momentum of the event. For more details see ref. [24].

We define a "low-Q^2" sample consisting of events which have the scattered electron in the backward calorimeter, ($160° \lesssim \theta_e \lesssim 172.5°$, $Q^2 \lesssim 80$ GeV^2), and a "high Q^2" sample consisting of events which have the electron scattered into the LAr calorimeter ($\theta_e \lesssim 155°$, $Q^2 \gtrsim 100$ GeV^2). A cut on y is applied ($y < 0.5$ and $y < 0.7$ in the low and high Q^2 samples, respectively) in order to avoid regions in which QED corrections and residual photoproduction background may be large. A cut on the hadronic invariant mass of $W^2 > 5000$ GeV^2 ensures a substantial hadronic energy flow in the detector. Fig. 9a and 9b show uncorrected data on fractional jet rates for 1+1, 2+1, and $\geq$ 3+1 jet events as a function of the jet resolution parameter y_{cut}, for the low and high Q^2 sample respectively.

Three different prescriptions for the simulation of QCD effects in deep inelastic scattering are compared to our data:

- Quark parton model and leading log parton showers.

- $O(\alpha_s)$ matrix elements with matched parton showers.

- The colour dipole model.

The leading log parton shower models used are LEPTO 5.2 [25], labelled PSWQ, and HERWIG 5.5 [26], labelled HERWIG. For $O(\alpha_s)$ matrix elements with matched parton showers the model in LEPTO 6.1 [27], labelled MEPS was used. Finally the colour dipole model calculations were obtained using ARIADNE 4.03 [28] (as implemented in LEPTO 6.1, i.e. $O(\alpha_s)$ matrix elements for boson gluon fusion and colour dipole radiation), labelled CDM. Note that all models, except for HERWIG, use the same LUND fragmentation scheme [29]

for hadronization. For all distributions the MRSD0 [30] parton distributions were assumed for the proton. In case of the PSWQ approach, the amount and hardness of the gluon radiation depends sensitively on the virtuality of the parton before and after the quark-photon vertex. For the present analysis we have used $Q \cdot W$ as a scale, guided by earlier H1 results which have excluded both Q^2 and W^2 scales for parton showers as implemented in the LEPTO program [31].

The MEPS model describes the jet rates best. It has been found that the jet rates at the level of partons, hadrons, and after detector simulation differ by less than 15% for jet resolutions $y_{cut} \geq 0.02$. HERWIG gives a fair description at low Q^2 but does not properly describe the multi-jet rate at high Q^2. Both PSWQ and CDM predict too high multi-jet rates at low Q^2.

Fig. 10a shows the fractional 2+1 jet rate as a function of the momentum transfer Q^2. We observe the expected rise with Q^2 due to the increased phase space for multi-jet production. The MEPS model gives a good description of the data, while PSWQ predicts a too high 2+1 jet rate. HERWIG and CDM fail to describe the rise with Q^2.

Since the rate of 2+1 jet events is proportional to α_s, the Q^2 dependence of the 2+1 jet rate is sensitive to the Q^2 variation of α_s. Fig. 10b shows the 2+1 jet rate as a function of Q^2 compared to the MEPS model with running α_s and constant α_s. Although with the present data no discrimination is possible, it can be seen that the slope of the Q^2 variation of the 2+1 jet rate is sensitive to the running of α_s.

4.2 Rapidity Gap Events

In studying the hadronic final state of the deep inelastic events, we found that the majority of events with the produced quark jet at large angle have a significant energy flow at smaller angles (in the proton direction). This energy flow is shown in Fig. 11 together with predictions of the models introduced above. The data are not corrected for detector smearing; the model predictions are given after full detector simulation and reconstruction. The models follow roughly the trend of the data: the energy flow in the forward region results from proton remnant fragmentation, initial state radiation and colour string effects [31]. However, the models do not describe the energy flow in detail. It is not yet clear if this can be improved by additional tuning of the model parameters, or if more fundamental ingredients necessary to describe the remnant fragmentation and initial state radiation are missing in the present Monte Carlo programs.
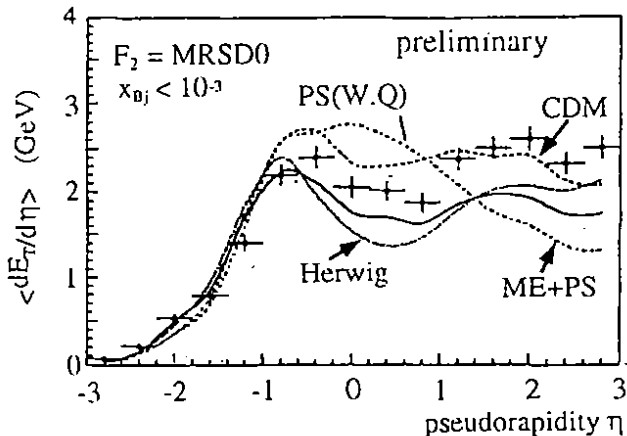
Figure 11: Average weighted energy flow $< dE_T/d\eta >$ as a function of the laboratory pseudorapidity η. The models are described in the text

In the data a fraction of events was found which shows no significant energy deposit outside of the produced quark jet region, i.e. no energy is detected around the beampipe in the proton remnant direction. Thus, these events exhibit an "empty gap" between the struck quark and the proton remnant. The maximum pseudorapidity, $\eta = -\ln(\tan\theta/2)$, for energy clusters measured in our calorimeter is 3.8. A class of 'rapidity gap' events is defined by asking that no energy cluster with $E_{clust} > 400\ MeV$ is found for $\eta > 1.8$, i.e. that there be a gap of at least 2 units in pseudorapidity. In the deep inelastic sample we find that 6% of the events exhibit such a rapidity gap while calculations made with the LEPTO 6.1 Monte Carlo generator [27] predict only 0.1%. Fig. 12 shows some characteristics of these events, including the rapidity gap distribution, the invariant mass (M_x) spectrum of the hadronic final state measured in the detector and the ratio $R(Q^2)$ of DIS events with a gap larger than 2 units to all DIS events as a function of Q^2. The distributions are not corrected for detector acceptance effects. The rapidity gap distribution shows clearly the two different types of events. The part for $\Delta\eta < 1$ is well described by the Monte Carlo. The invariant mass M_x is in general quite small. Note that the region below 4 GeV is strongly affected by the detector acceptance. $R(Q^2)$ does not – within the limited statistics – depend significantly on Q^2. The apparent "color disconnection" between the proton remnant and struck quark, and the M_x distribution suggest that the underlying process is diffractive-like, although other scenarios e.g. pion exchange cannot be ruled out yet. It will be interesting to
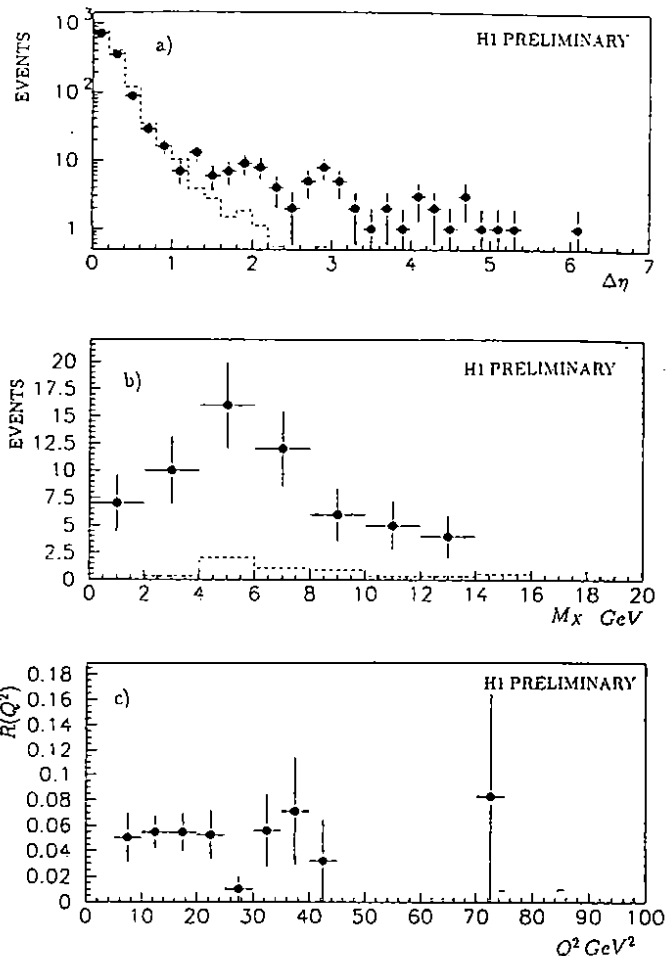

Figure 12: a) Distribution of the rapidity gap $\Delta\eta$ for DIS events; b) Invariant mass of the visible hadronic system for events with $\Delta\eta > 2$; c) Ratio $R(Q^2)$ of events with a rapidity gap $\Delta\eta > 2$ over all DIS events, as function of Q^2.

study these events in detail, since they may be linked to hard diffraction [32] possibly giving information on the Pomeron structure function.

5 Proton Structure Function at Low x

One of the main physics topics at HERA is the exploration of the structure of the proton in the newly accessible Q^2 and x region. Precise QCD tests will be possible in the high Q^2 regime, but are at present hampered by the limited available statistics. With the present data we can study the low-x region down to values of 10^{-4}, while still staying in the DIS regime. At these low x values new QCD effects like saturation and gluon recombination could become visible. The present analysis measures for the first time the structure function $F_2(x, Q^2)$ in this small x region.

9

Structure function measurements are a key ingredient for the determination of parton distributions of nucleons. Precise knowledge of parton distributions is important e.g. for the calculation of production processes in hadronic interactions which can be described by perturbative QCD. Since future high energy colliders will be sensitive to x values of $O(10^{-3})$, measurements at HERA will be a key input for understanding the production rates. Moreover, the dynamics that generates parton distributions at low-x is a field of strong theoretical interest. In particular, novel perturbative QCD effects are expected to show up at x values below 10^{-3}.

5.1 Experimental Procedure

With the available luminosity a meaningful structure function determination is limited to values of $Q^2 < 100$ GeV^2. Therefore we have restricted the analysis to those electrons which are scattered into the backward electromagnetic calorimeter (BEMC) at a polar angle of less than about 160°. Preliminary $F_2(x, Q^2)$ measurement at large Q^2 where the electron is scattered in the LAr Calorimeter are presented in [33]. Since the lever arm in Q^2 is rather limited, we present the $F_2(x, Q^2)$ measurement as function of x for given Q^2 values rather than as a function of Q^2 for given x values.

The current results were obtained by two independent methods. In the first – termed method I – the event kinematics was calculated from the scattered electron variables E'_e and θ_e only, according to eqn. (2). The cross sections and related efficiencies were determined in $\sqrt{E'_e}, \theta_e$ bins which match the resolution and acceptance of the detector. The calculated cross sections in these detector oriented bins were then transformed to cross sections in x and Q^2. In the second method – termed method II – bins in x, Q^2 were used for cross section and efficiency calculations. Information on both the scattered electron and hadronic final state was used to determine the event kinematics. The Q^2 value was determined from the electron variables only, using equation (2), but y was determined from the hadrons, using equation [34]:

$$y_h = \sum_{hadrons} \frac{E_h - p_{z,h}}{2E_e},\qquad (4)$$

where E_h is the energy of a hadron and $p_{z,h}$ its momentum component along the incident proton direction. The kinematical region used for the analysis was $\theta_e < 172.5^0$ and $E'_e > 10.4\ GeV$. Method II is further restricted to the region $x < 0.02$ and $y_h < 0.3$. These limits ensure that a large fraction of the energy of the produced quark jet is contained in the LAr calorimeter.

The two methods differ further in the $\gamma - p$ background subtraction, usage of simulated data and elec-tron identification. Methods I and II use different parts of the detector to calculate the event kinematics and the necessary radiative corrections are quite different. The observed agreement between the structure functions of both analyses represents therefore an important cross check of our measurements.

A clean sample of deep inelastic scattering candidates is selected offline by requiring an electron candidate (hit in the BPC; electromagnetic shower in the BEMC) and an event vertex in the interaction region. The resulting event sample contains not only Born events, but also so called radiative events. Examples are events with real photons emitted by the electron before or after the boson exchange with the proton. The measured cross sections have to be corrected for these effects. To reduce the radiative corrections and also the photoproduction background the missing energy in the backward direction, $E_{miss} = E_e \cdot (y_e - y_h)$, is required to be smaller than 11.7 GeV for the method I. More details on the experimental procedure are given in [35].

After all cuts about 1,000 events are left in the data samples. From electron tagger studies and extensive photoproduction Monte Carlo studies we conclude that the overall remaining photoproduction contamination is less than 2%, and less than 30% for the lowest x datapoints presented here. The remaining background was subtracted statistically. From pilot bunch studies we conclude that the amount of beam induced non-ep background, e.g. from protons with rest gas in the interaction region, is less than 1% overall. The efficiencies of the applied cuts have been determined from studies of the data. Acceptance and smearing corrections were determined from detailed simulation of large event samples, using different Monte Carlo generator programs and different assumptions for the a priori unknown structure function. The resulting differences in acceptance corrections were included in the systematic errors of the data points. Radiative corrections were applied using numerical calculations from TERAD91[36] or the Monte Carlo program HERACLES[37].

5.2 The Structure Function $F_2(x, Q^2)$

The Born cross section for deep inelastic electron scattering off a proton can be expressed in terms of the structure function F_2 and the photoabsorbtion cross section ratio of longitudinally and transversely polarised photons, $R = \sigma_L/\sigma_T$:

$$\frac{d^2\sigma}{dxdQ^2} = \frac{2\pi\alpha^2}{Q^4 x}\left(2\,(1 - y)\ +\ \frac{y^2}{1 + R}\right) F_2(x, Q^2),\quad (5)$$

for $Q^2 << M_Z^2$. The ratio $R(x, Q^2)$ has not yet been measured at HERA. Therefore, in order to extract F_2

from the measured differential cross section, an assumption for R has to be made. We have chosen R values calculated according to the QCD prescription [38] using the MRSD– parton distributions. Note that R contributes to the differential cross section mainly in the high y region. In the region of our measurement the chosen R values reduce the cross section by at most 8% compared to assuming $R = 0$.
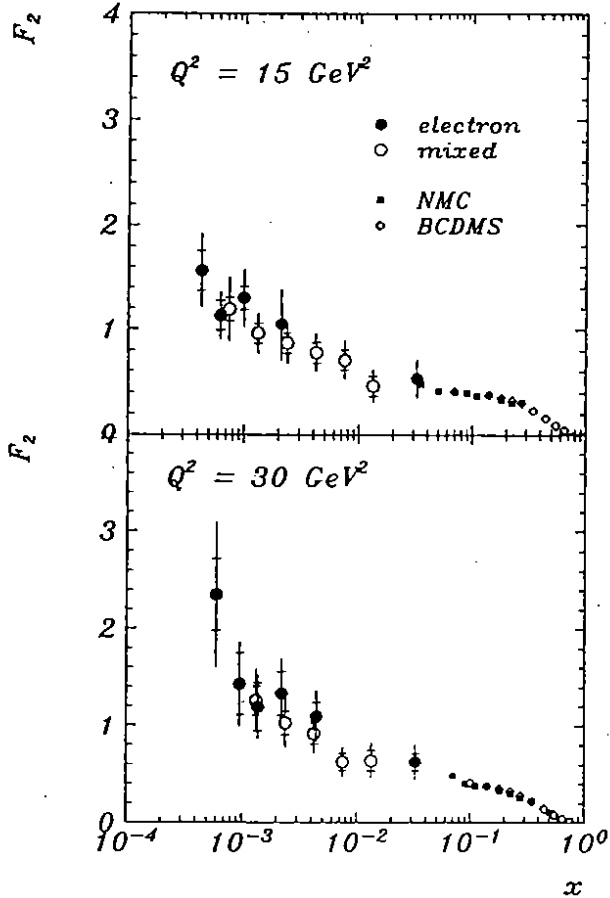

Figure 13: Measurement of $F_2(x, Q^2)$ for two values of Q^2. The full circles correspond to method I (electron measurement), while the open circles correspond to method II (mixed variable measurement). The error bars show statistical and total errors obtained by adding the statistical and systematic errors in quadrature. In addition all points have a normalization uncertainty of 8%. Data points of the fixed target muon proton scattering experiments NMC and BCDMS are shown for comparison.

The results of method I "electron" and of method II "mixed" are found to be in excellent agreement as is shown in Fig. 13. Also shown are the NMC[39] and BCDMS[40] measurements. The high x data points agree well with the available measurements from fixed target experiments giving us an independent cross-check of the absolute normalization with an accuracy of $\sim$ 20%.
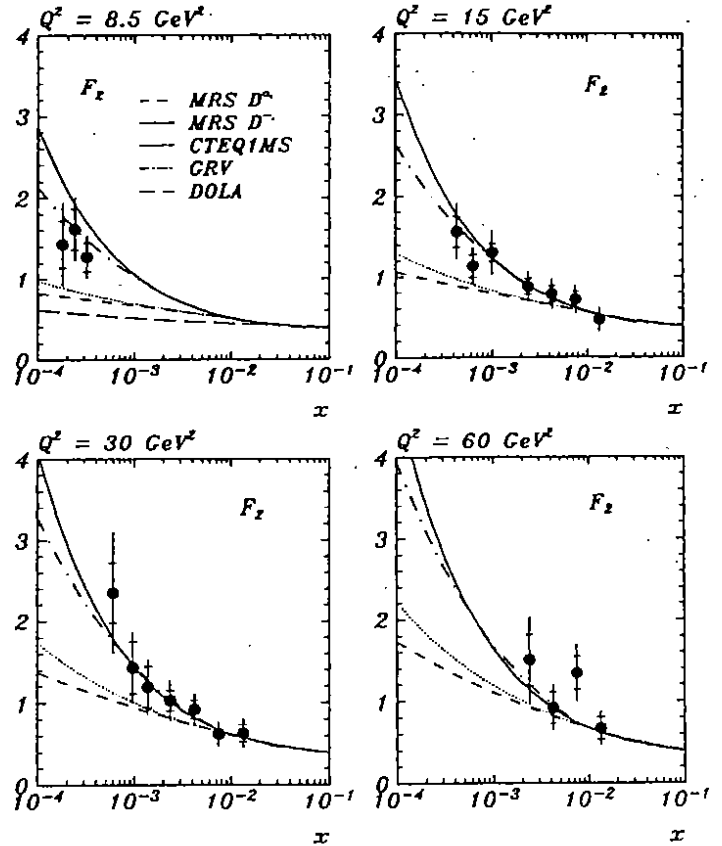

Figure 14: The measured structure function $F_2(x, Q^2)$ for different values of Q^2, compared to several structure function parametrizations which are fitted to recent low energy data, described in the text. The error bars show statistical and total errors obtained by adding the statistical and systematic errors in quadrature. In addition all points have a normalization uncertainty of 8%.

The final measured $F_2(x, Q^2)$ is presented in Fig. 14 for four values of Q^2, 8.5, 15, 30 and 60 GeV^2. The systematic errors range from 15% to 25% The calculation of the systematic uncertainty included the following error sources: possible shifts of the electron energy scale by 2% (20% at largest x for method I) and of θ_e by 5 mrad (8%); uncertainty of y_h (25% at lowest x for method II); uncertainties in the selection efficiency calculations (10%); electron and proton beam induced background (4% for lowest x); photoproduction contamination in

11

the lowest x bin (10%); the influence of different structure functions and hadronization uncertainties on the acceptance calculation (10% at most); the bin centre correction (5%); radiative corrections (8% at lowest x for the electron method). Additionally, not shown, there is a global 8% normalization uncertainty on each data point, resulting mainly from the uncertainty of the luminosity measurement.

At low x the $F_2(x, Q^2)$ is seen to rise with decreasing x. The extrapolations/predictions of different parton distributions are compared with the data. The GRV[41] and MRSD$-$'[42] distributions are found to describe the data quite well, while the CTEQ1MS[43] and MRSD0' distributions are significantly below the data. For the GRV distribution the rise of the parton density at small x is generated dynamically, while for the MRSD$-$' distribution a Lipatov $1/\sqrt{x}$ type of behaviour is assumed for the gluon at small x. The CTEQ1MS distribution assumes a Lipatov behaviour of the gluon too, but for this parametrization the sea quark distributions are not strongly coupled to the gluon distribution. It turns out that the predicted sea quark distribution at small x is rather flat and hence the resulting $F_2(x, Q^2)$ is not very different from the MRSD0' prediction. The parametrization of Donnachie and Landshoff (DOLA) [44] is a Regge theory motivated fit, which is applicable for Q^2 values up to about 10 GeV^2. This parametrization clearly undershoots the data.

It is tempting to conclude that the measurements of $F_2(x, Q^2)$ indicate the observation of Lipatov behaviour at small x. However, to establish this unambiguously a careful analysis of the $F_2(x, Q^2)$ evolution at different Q^2 values with more precise data needs to be made. Additional information, e.g. from DIS events with associated high x jets will be needed to establish or support this picture. It is in any case encouraging to see $F_2(x, Q^2)$ rise at small x, since this means that the parton saturation regime can be reached earlier, possibly already at HERA at somewhat smaller x values than presented in this analysis. The result suggests that there is much exciting physics to be done at HERA.

6 Beyond the Standard Model

HERA is an ideal machine to look for leptoquarks (gluons) and excited leptons, which can be produced either by fusion of the incoming lepton with a quark (gluon) of the proton, or fusion of the lepton with an exchanged boson. Sofar no candidates have been found for any of these channels. Limits have been deduced (see ref. [45,46]) which depend on the coupling. For couplings as large as the electromagnetic coupling, the excluded mass range is typically below 190 GeV for var-

ious types of scalar and vector leptoquarks. New limits for excited electrons are shown in Fig. 15, updated compared to [45] with information on decay channels including jets.

A search for R-parity violating supersymmetric squarks has been made. In the accessible range of couplings, the squarks have mainly leptoquark-like signals. The rejection limits obtained for leptoquarks can be re-interpreted as a function of the squark masses. The results are shown in Fig. 16.
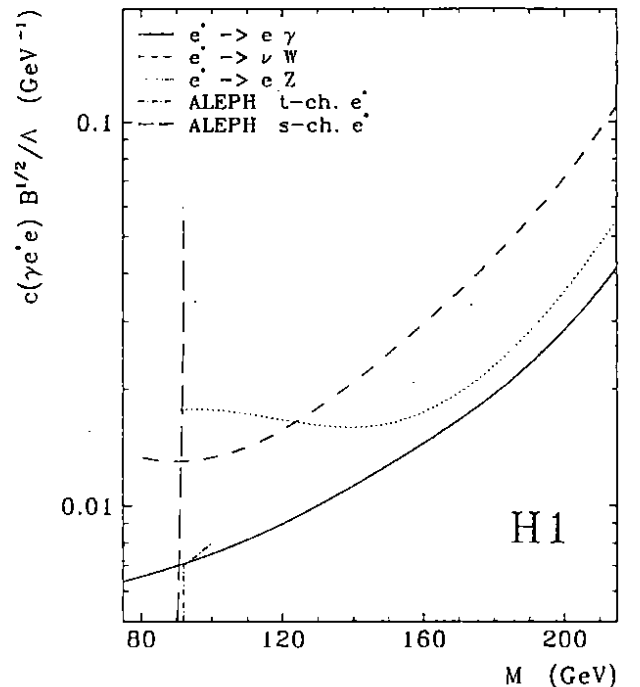

Figure 15: Rejection limits with a CL of 95% for the e^*. Regions above the curve are excluded.

7 Conclusion

New results from the H1 experiment on photoproduction, deep inelastic scattering and search for exotics have been presented. In the photoproduction sector it was shown that the total photoproduction cross section rises only slowly with energy. Hard scattering has been observed in $\gamma - p$ collisions, and jet cross sections have been measured. The x_γ distribution, determined from 2-jet events, shows a clear sensitivity to the gluon component in the photon. Parton distribution parametrizations assuming a large gluon component at large x_γ are disfavoured.
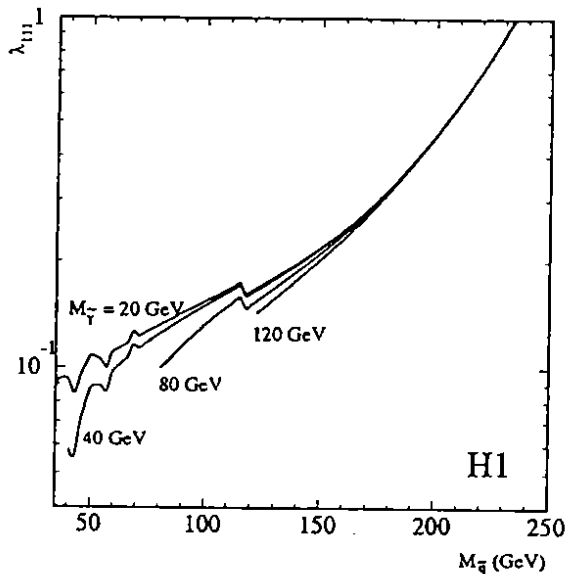
Figure 16: Rejection limits at the 95% CL for the coupling λ_{111} as a function of the squark mass for various fixed photino masses. The region above the curve is excluded. The limit combines all charged and neutral decays of the $\bar{d}$ and $\bar{u}$.

Final states in DIS have been studied. Events with clear multi-jet topologies have been observed. Multi-jet rates have been measured and compared to QCD inspired models. Events were isolated which show a large empty gap between the struck quark and the proton remnant. These events exhibit diffractive like characteristics. The proton structure function $F_2(x, Q^2)$ has been measured in the newly accessible region of low x. The results show a strong rise of $F_2(x, Q^2)$ with decreasing x for $10^{-4} < x < 10^{-2}$. Finally, new exclusion limits were given for excited electrons and squarks.

8   Acknowledgements

References

[1] B.H. Wiik, *Recent Developments in Accelerators*, these proceedings.

[2] J.Bartels and J.Feltesse, Proceedings of the Workshop "Physics at HERA", ed. W. Buchmüller and G. Ingelman, Hamburg (1992) 133; Workshop on Deep Inelastic Scattering, April 1992, Teupitz, Germany, J. Blümlein and T. Riemann editors.
E.M. Levin, Proceedings of the Internatinal Conference on "QCD, 20 years later", ed. P.M. Zerwas and H.A. Kastrup, Aachen (1992).

[3] H1 Collab., *The H1 Detector at HERA*, to be submitted to Nuclear Instruments & Methods.

[4] H1 Calorimeter Group, B. Andrieu et al., NIM A 336 (1993) 460.

[5] H1 Calorimeter Group, B. Andrieu et al., NIM A 336 (1993) 499.

[6] G. Yodh, Nucl. Phys. B (Proc. Suppl.) 12 (1990) 277.

[7] A. Rostovtsev, *Hard Photoproduction at HERA*, these proceedings.

[8] W. Bartel, *Total photoproduction cross section and Diffraction*, these proceedings.

[9] C.F Weizsäcker, Z. Phys. 88 (1934) 612; E.J. Williams Phys. Rev. 45 (1934) 729.

[10] ZEUS Collab., M. Derrick et al, Phys.Lett. 293B (1992) 465.

[11] A.Donnachie and P.V.Landshoff, Phys.Lett. 296B (1992) 277.

[12] H.Abramovicz et al., Phys.Lett. 269B (1991) 465.

[13] F.M. Borzumati et al., DESY preprint 93-034 (1993)

[14] H1 Collab., I. Abt et al., *Measurement of Inclusive Jet Cross Sections in Photoproduction at HERA*, DESY preprint 93-100

[15] H. Bengtsson and T. Sjöstrand, Comp. Phys. Comm. 46 (1987) 43; T. Sjöstrand, CERN-TH-6488-92 (1992).

[16] H. Abramowicz, K. Charchula, A. Levy, Phys. Lett. 269B (1991) 458.

[17] M. Glück, E. Reya, A.Vogt, Phys. Rev. D46 (1992) 1973.

[18] EMC Collab., J.J. Aubert et al., Phys. Lett. 95B (1980) 306, Phys. Lett. 100B (1981) 433, Phys. Lett. 119B (1982) 233.

[19] EMC Collab., M. Arneodo et al., Z. Phys. C36 (1987) 527.

[20] E665 Collab., M.R. Adams et al. Phys. Rev. Lett. 69 (1992) 1026.

[21] B. Andersson et al., Z. Phys. C9 (1981) 233, G. Ingelman et al., Nucl. Phys. B206 (1982) 239.

[22] I.H. Park, *Jets in Deep Inelastic Scattering* , these proceedings.

[23] JADE Collab., W. Bartel et al., Z. Phys. **C33** (1986) 23.

[24] H1 Collab., I. Abt et al., *A measurement of Multijet Rates in DIS at HERA* DESY preprint 93-137

[25] G. Ingelman, "LEPTO 5.2", unpublished program manual;
H. Bengtsson, G. Ingelman, and T. Sjöstrand, Nucl. Phys. **B301** (1988) 554.

[26] G. Marchesini et al., Comp. Phys. Comm. **67** (1992) 465, and references therein.

[27] G. Ingelman, "LEPTO 6.1", Proceedings of the Workshop "Physics at HERA", ed. W. Buchmüller and G. Ingelman, Hamburg, (1992), 1366, and references therein.

[28] L. Lönnblad, ARIADNE version 4.03, Comp. Phys. Commun. **71** (1992) 15, and references therein.

[29] T. Sjöstrand, Comp. Phys. Commun. **39** (1986) 347;
T. Sjöstrand and M. Bengtsson, Comp. Phys. Commun. **43** (1987) 367, and for JETSET 7.3, CERN-TH. 6488/92 (1992).

[30] A. D. Martin, W. J. Stirling, R. G. Roberts, Phys. Rev. **D47** (1993) 867.

[31] H1 Collab., T. Ahmed et al., Phys. Lett. **298B** (1993) 469.

[32] G. Ingelman and P.E. Schlein, Phys. Lett. **152B** (1985) 256;
A. Donnachie, P.V. Landshoff, Phys.Lett **191B** (1987) 309;
M. G. Ryskin, Sov. J. Nucl. Phys. **53** (1991) 668.

[33] G. Bernardi *The H1 Structure Function Measurement*, these proceedings.

[34] A. Blondel and F. Jacquet, Proceedings of the Study of an *ep* Facility for Europe, ed. U. Amaldi, *DESY* **79-48** (1979) 391.

[35] H1 Collab., I. Abt et al., Nucl. Phys. **B407** (1993) 515.

[36] A. Akhundov et al., Proc. Workshop "Physics at HERA", ed. W. Buchmüller and G. Ingelman, Hamburg, (1991) 1285.

[37] A.Kwiatkowski, H.Spiesberger, and H.-J.Möhring, Comp. Phys. Commun. **69** (1992) 155, and references therein.

[38] G. Altarelli, G. Martinelli, Phys.Lett. **76B** (1978) 89.

[39] NMC Collab., P. Amaudruz et al., Phys. Lett. **295B** (1992) 159 and Erratum to CERN-PPE/92-124, CERN, April 1993.

[40] BCDMS Collab., A.C. Benvenuti et al., Phys.Lett. **223B** (1989) 485.

[41] M. Glück, E. Reya and A. Vogt, Z. Phys. **C53** (1992) 127;
M. Glück, E. Reya and A. Vogt, Phys. Lett. **306B** (1993) 391.

[42] A. D. Martin, W. J. Stirling, R. G. Roberts, Phys.Lett. **306B** (1993) 145, Erratum **309B** (1993) 492.

[43] J. Botts et al., Phys. Lett. **304B** (1993) 159.

[44] A. Donnachie, P. V. Landshoff, M/C-th 93/11, DAMTP 93-23.

[45] H1 Collab., T.Ahmed et al., Nuclear Physics **B396** (1993).

[46] F. Raupach, *Search for leptoquarks, leptogluons, excited leptons, and squarks in H1 at HERA*, these proceedings.